Chemical Science

ROYAL SOCIETY OF CHEMISTRY

EDGE ARTICLE

View Article Online
View Journal

Cite this: DOI: 10.1039/d6sc02382g

All publication charges for this article have been paid for by the Royal Society of Chemistry

Minimum effort, maximum effect: modulating twisted intramolecular charge transfer for ultralong room temperature phosphorescence

Wu-Jie Guo,† Shirong Yan,† Shihao Xu, Tongfei Qi and Hui-Qing Peng *

Achieving efficient organic ultralong room temperature phosphorescence (OURTP) hinges on populating and stabilizing triplet excitons. Herein, we demonstrate a "minimum effort, maximum effect" strategy by precisely modulating the twisted intramolecular charge-transfer (TICT) process in minimalist single-benzene luminophores (SBLs). A synergistic attenuation of steric hindrance in electron-donating groups and electron-withdrawing potency in accepting groups is shown to facilitate TICT formation. The resulting TICT state acts as a pivotal relay, efficiently narrowing the singlet–triplet energy gap (ΔE_{ST}) and enhancing spin–orbit coupling (SOC) to foster rapid intersystem crossing and triplet population. Subsequent stabilization of these triplet states is achieved through a rigid hydrogen-bonding network within a polyvinyl alcohol (PVA) matrix. This work establishes a direct correlation between TICT character and OURTP performance, revealing a molecular-level "butterfly effect", where subtle structural modifications yield dramatic photophysical enhancements. The findings provide a novel paradigm for designing high-performance OURTP materials from simple and compact molecular systems.

Received 23rd March 2026
Accepted 5th June 2026

DOI: 10.1039/d6sc02382g

rsc.li/chemical-science

Introduction

Pure organic ultralong room temperature phosphorescence (OURTP) has emerged as a promising candidate for next-generation optoelectronic devices, data encryption systems, and bioimaging probes due to its merits of millisecond-scale lifetime, large Stokes shift, and unique excited-state characteristics.[1–8] Despite these advantages, the practical development of efficient OURTP materials still faces fundamental challenges rooted in the spin-forbidden nature of intersystem crossing (ISC) and the high susceptibility of triplet excitons to nonradiative decay. The ISC efficiency critically determines the population of triplet excited states and follows the relationship:[9]

$$k_{ISC} \propto |\langle S|H_{SOC}|T\rangle|^2 \exp(-\Delta E_{ST}^2) \quad (1)$$

where both spin–orbit coupling (SOC) matrix elements and singlet–triplet energy gaps (ΔE_{ST}) serve as key parameters. Current strategies to enhance k_{ISC} primarily focus on two complementary approaches: (1) SOC enhancement through strategic incorporation of heavy atoms, heteroatoms, or aromatic carbonyls into the molecular skeletons[10–15] and (2) ΔE_{ST} reduction through donor–acceptor architectures that generate intramolecular charge-transfer (ICT) excited states.[16–20]

While conventional ICT configurations have demonstrated some success, their twisted counterparts (TICT systems) remain significantly underexplored for OURTP optimization despite offering distinct advantages in excited-state modulation. On one hand, the characteristic orthogonal donor–acceptor geometry in TICT systems can induce substantial orbital angular momentum redistribution, thereby promoting spin-flip processes.[21,22] On the other hand, compared to planar ICT configurations, TICT configurations demonstrate intensified charge separation character and decreased singlet-state energy levels, potentially yielding markedly reduced ΔE_{ST} values that further boost the ISC efficiency (Fig. 1a).[23,24] These inherent advantages position TICT manipulation as a cornerstone strategy for high-performance OURTP material design.

Emerging evidence suggests that the strategic selection of electron-donating (EDGs) and electron-withdrawing groups (EWGs) provides a powerful avenue for fine-tuning TICT characteristics.[25,26] Nevertheless, the development of clear structure–property relationships to enable precise control over triplet excitons and ultimate OURTP performance remains a considerable challenge. To address this, we propose that rational modulation of the steric and electronic properties of EDGs and EWGs in simple structures could serve as a fundamental molecular-level strategy to regulate triplet population dynamics. Concurrently, immobilization of these minimalist luminophores within a polymer matrix (*e.g.*, polyvinyl alcohol) offers a macroscopic complement by imparting structural rigidity to suppress nonradiative decay of triplet excitons.[27–30] The integration of these two approaches, namely molecular design through TICT engineering

State Key Laboratory of Chemical Resource Engineering, Beijing Advanced Innovation Center for Soft Matter Science and Engineering, Beijing University of Chemical Technology, Beijing 100029, China. E-mail: hqpeng@mail.buct.edu.cn

† W.-J. Guo and S. Yan contributed equally to this work.

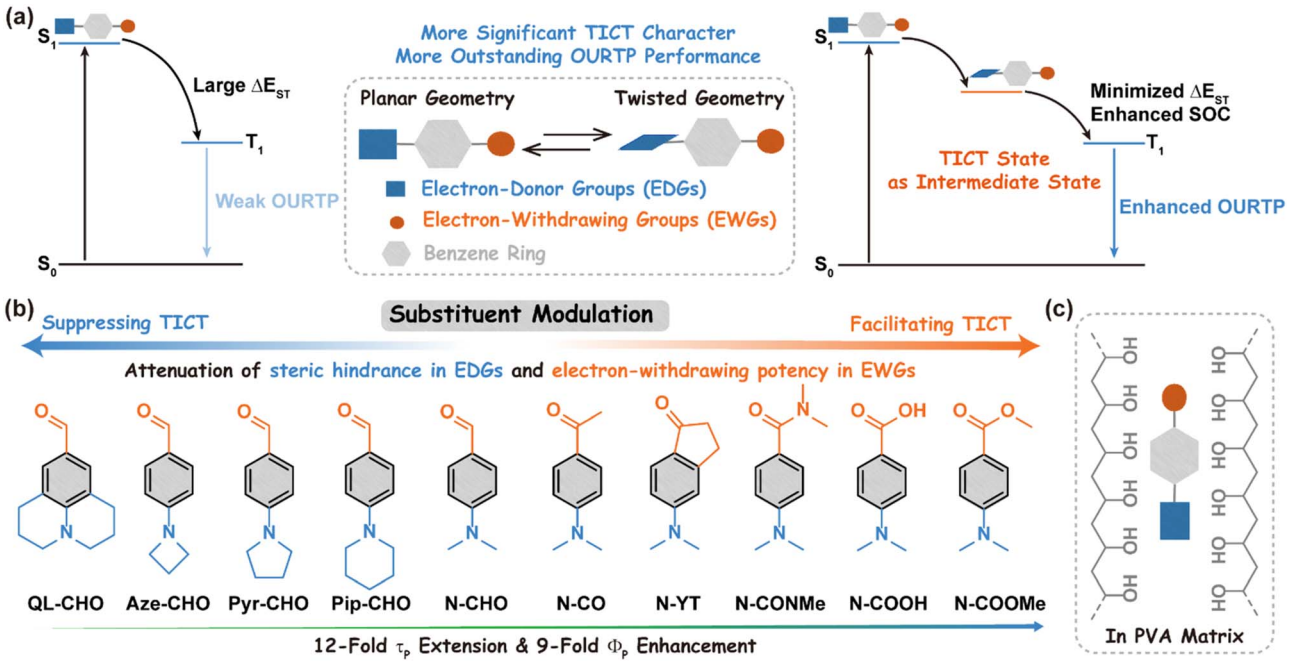

Fig. 1 (a) Illustration of the TICT state as an intermediate state for enhancing OURTP. (b) The chemical structures of single-benzene luminophores. (c) Illustration of the single-benzene luminophore in the PVA matrix.

together with macroscopic stabilization *via* matrix confinement, establishes a highly synergistic framework capable of achieving high efficiency in OURTP systems.

Based on the above hypothesis, we selected a library of single-benzene luminophores (**SBLs**) with modifying different dialkylamino groups as EDGs and carbonyl-containing substituents as EWGs (Fig. 1b). These structurally simplified guests were embedded into rigid polyvinyl alcohol (PVA) matrices to construct tunable OURTP systems, allowing for a direct and precise dissection of the correlation between TICT and OURTP (Fig. 1c). Controlled attenuation of the steric hindrance in EDGs and electron-withdrawing potency in EWGs produced striking performance enhancements, *viz.* phosphorescence lifetimes surged from 112 ms (**QL-CHO**) to 1368 ms (**N-COOMe**), while quantum yields increased from 3.2% to 29.6%, accompanied by a hypsochromic afterglow shift from green to blue (Fig. 2a and Table 1). Experimental results coupled with theoretical calculations revealed a direct proportionality between the enhancement of OURTP and the TICT formation capacity. The lowered energy barrier (E_{EB}) from 0.22 eV (**N-CHO**) to −0.76 eV (**N-COOMe**) through the synergistic EDG and EWG modifications enabled enhanced dialkylamino rotor motion, which improved TICT-driven ΔE_{ST} reduction and SOC intensification. This dual modulation establishes TICT states as potent intermediate gateways for triplet exciton accumulation. The resultant materials exhibit intriguingly afterglow tunability and show promising potential in dynamic information encryption and flexible afterglow displays.

Results and discussion

A series of ten **SBLs** with different dialkylamino donors and carbonyl acceptors were employed, in which synthesized derivatives 5-(dimethylamino)-2,3-dihydro-1*H*-inden-1-one (**N-YT**) and 4-(dimethylamino)-*N*,*N*-dimethylbenzamide (**N-CONMe**) were characterized by ^{1}H NMR spectroscopy, ^{13}C NMR spectroscopy, and high-resolution mass spectrometry, while other commercial compounds were purified through dichloromethane/petroleum ether recrystallization (see Fig. S1–S6 and the SI for details). These compounds, including julolidine-based **QL-CHO**, dimethylamino-modified **N-CHO**, and ester-functionalized **N-COOMe**, were embedded in PVA matrices by drop-casting their aqueous mixture onto a quartz substrate followed by heating to remove water. This process facilitates the formation of rigid host–guest film architectures (**SBL@PVAs**) through hydrogen bonding between the guest molecules and the PVA matrix. The optimal doping concentration (1 wt%) of guest molecules in PVA was determined by taking **N-CHO** as an example *via* comprehensive evaluation of its corresponding phosphorescence intensity, lifetime, and film transparency (Fig. S7). As shown in Fig. 2a, these doped films can exhibit tunable afterglow emission ranging from blue to green after being appropriately excited by UV light at either 254 nm or 365 nm (Fig. S8).

Photophysical analysis revealed dual emission characteristics across all **SBL@PVAs** in the prompt spectra (Fig. 2b). The short-wavelength emissions with nanosecond-level lifetimes (τ = 1–3 ns) were identified as fluorescence (Fig. S9 and Table 1). However, time-gated measurements (1 ms delay) confirmed the phosphorescent nature of the long-wavelength emission bands, which exhibited millisecond lifetimes (τ = 112–1369 ms) and quantum yields up to 29.6% (Fig. 2b–e and Table 1). Two interdependent substituent effects, with a focus on EDGs and EWGs, had pronounced impacts on these OURTP enhancements. With the guest changing from **QL-CHO** to **N-CHO**

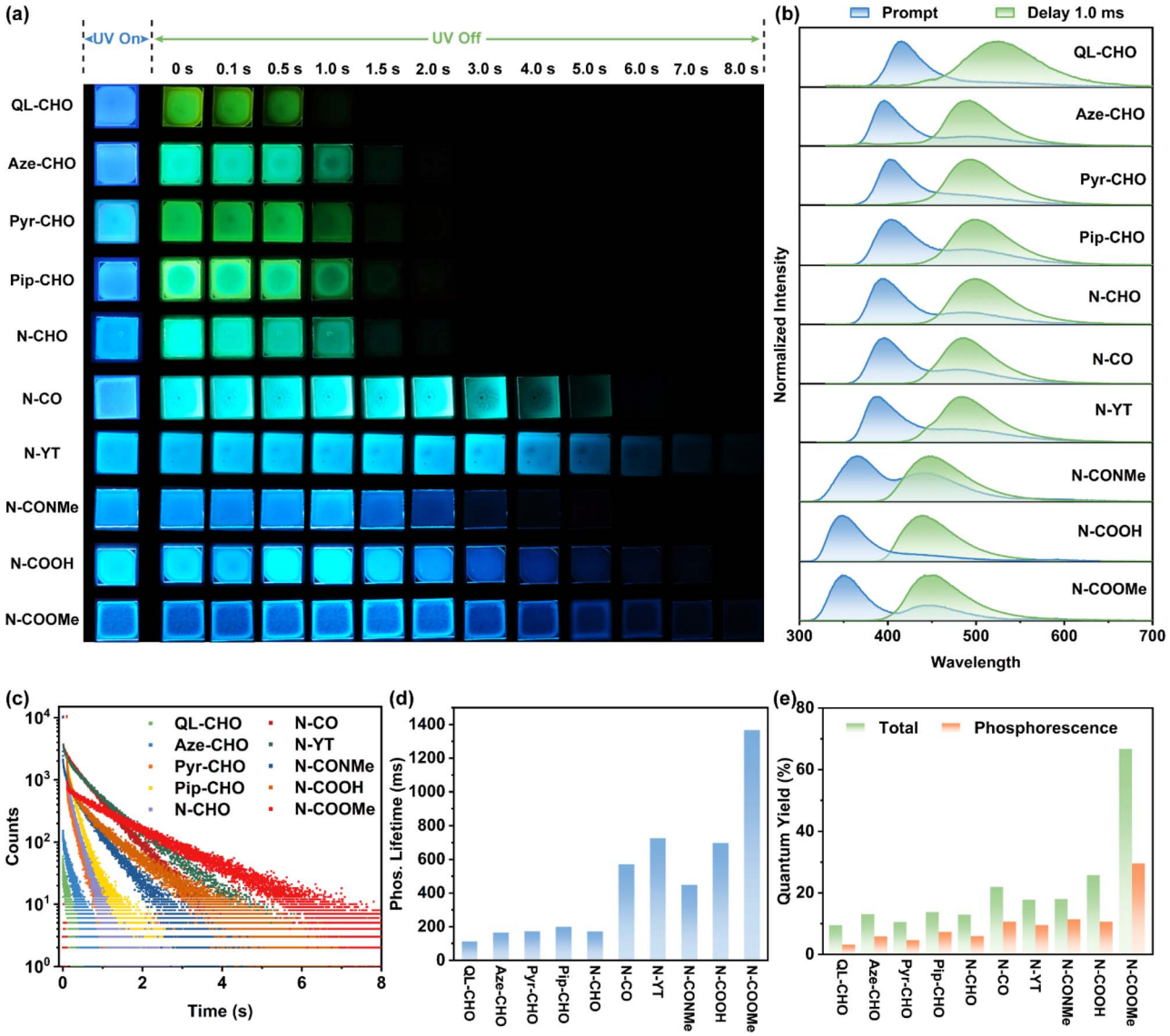

Fig. 2 (a) Photographs of SBL@PVAs under UV irradiation and after turning off the UV light. (b) The normalized prompt and delay emission spectra (delay time = 1 ms). (c) The phosphorescence decay curves, (d) the phosphorescence lifetimes, and (e) the total photoluminescence quantum yields and phosphorescence quantum yields of SBL@PVAs.

Table 1 Photophysical properties of SBL@PVAs

Compound	λ_F/nm	τ_F/ns	Φ_{Total}/%	λ_P/nm	τ_P/ms	Φ_P/%	k_{ISC}/s^{-1} [a]	k_r^P/s^{-1} [b]	k_{nr}^P/s^{-1} [c]
QL-CHO	419	0.65	9.4	523	112	3.2	4.88×10^7	0.28	8.65
Aze-CHO	400	1.03	13.0	492	165	5.9	5.75×10^7	0.36	5.70
Pyr-CHO	400	1.16	10.5	494	173	4.6	4.00×10^7	0.27	5.51
Pip-CHO	400	1.66	13.7	500	199	7.4	4.44×10^7	0.37	4.65
N-CHO	400	1.16	13.0	500	171	6.0	5.15×10^7	0.35	5.50
N-CO	393	1.98	21.9	486	571	10.6	5.37×10^7	0.19	1.56
N-YT	393	2.77	17.8	484	726	9.6	3.45×10^7	0.13	1.25
N-CONMe	365	1.31	18.1	449	450	11.5	8.78×10^7	0.26	1.97
N-COOH	350	2.46	25.8	440	697	10.6	4.31×10^7	0.15	1.28
N-COOMe	358	2.01	66.7	450	1368	29.6	1.47×10^8	0.22	0.51

[a] The apparent k_{ISC} was estimated according to $k_{ISC} = \Phi_{ISC}/\tau_F \approx \Phi_P/\tau_F$. [b] $k_r^P = \Phi_P/\tau_P$. [c] $k_{nr}^P = (1 - \Phi_P)/\tau_P$.

system, the phosphorescence lifetime and quantum yield of **SBL@PVAs** increased by 53% and 88%, respectively (Table 1). It is worth noting that the transition from **QL-CHO** to **N-CHO** system demonstrated the progressively liberating dialkylamino group rotation through controlled alkyl chain cyclization, which was consistent with changes in phosphorescence properties of **SBL@PVAs**. Simultaneously, strategic attenuation of the electron-withdrawing capacity along the CHO → COMe → COOMe series induced 50 nm hypsochromic shifts while boosting phosphorescence lifetimes and quantum yields by factors of 8 and 5, respectively. The systematic control of both steric and electronic parameters through simple and straightforward substituent engineering established an unprecedented structure–property paradigm that enabled the optimization of TICT-mediated OURTP within minimalist molecular frameworks.

Notably, the spatially separated donor–acceptor geometry of the TICT state may intrinsically weaken the radiative transition probability compared with the planar ICT state. However, the rate analysis suggests that the phosphorescence radiative decay rate (k_r^P) exhibits only marginal variation across the series, indicating that it is unlikely to be the dominant factor governing the observed phosphorescence performance (Table 1). By contrast, the apparent intersystem crossing rate (k_{ISC}) increases from 5.15×10^7 s^{-1} for **N-CHO** to 1.47×10^8 s^{-1} for **N-COOMe**, while the phosphorescence nonradiative decay rate (k_{nr}^P) decreases from 5.50 s^{-1} to 0.51 s^{-1}. These results suggest that the ultralong lifetime and relatively high phosphorescence quantum yield are more closely associated with enhanced triplet-state population and effective suppression of triplet-state nonradiative deactivation, rather than to substantial modulation of the k_r^P.

To elucidate the origin of the OURTP properties, further characterization studies were carried out on the doped films, crystals, and solutions of these **SBLs**. Powder X-ray diffraction (XRD) analysis confirmed the amorphous nature of **SBL@PVAs**, eliminating their crystalline matrix contributions (Fig. S10). At 77 K, **SBLs** in dilute 2-methyltetrahydrofuran exhibited emission profiles comparable to those of the corresponding doped films, indicating that the phosphorescent nature inherent to **SBL@PVAs** originated from the **SBLs** themselves (Fig. S11 and S12). Moreover, we obtained the crystalline counterparts of **N-CHO**, **N-CO**, and **N-COOMe** (Table S1). Multiple C═O···H interactions were observed in these crystals, suggesting the potential for forming a hydrogen-bonding network involving these **SBLs** in the hydroxyl-rich PVA matrix (Fig. S13). Additionally, these crystals displayed redshifted emission and reduced lifetimes, providing direct evidence that molecular isolation within PVA effectively suppressed aggregation-caused photoluminescence quenching (Fig. S14). Replacing PVA with the hydrogen-deficient poly(methyl methacrylate) (PMMA) polymer led to **SBLs** showing negligible phosphorescence intensity and lifetime compared to **SBL@PVAs** (Fig. S15 and S16), highlighting the critical role of PVA in enabling noncovalent molecular immobilization through hydrogen bonding for efficient OURTP. ^{1}H NMR measurements further supported this hydrogen-bond-assisted incorporation, as the **N-CHO**, **N-CO**, and **N-COOMe** proton signals showed slight upfield shifts upon doping into PVA, indicating a PVA-induced microenvironmental change (Fig. S17).

Furthermore, we examined the absorption and fluorescence spectra of isolated **SBLs** in various solvents. All spectra exhibited a clear red shift with increasing solvent polarity, demonstrating pronounced solvent effects (Fig. 3a, S18 and S19). In particular, except for **QL-CHO** and **Aze-CHO**, the fluorescence spectra of other **SBLs** in highly polar solvents (*i.e.*, acetonitrile) showed dual emission characteristics. As shown in Fig. 3b–d, S20, Tables S2 and S3, the correlation between the Stokes shift of the two emission bands and solvent orientation polarizability (Δf) was then estimated, in which the long-wavelength emission (A band) exhibited a larger slope of the linear correlation between the Stokes shift (ν_a–ν_A) and Δf than that of the short-wavelength fluorescence (B band). This observation demonstrated that the A band resulted from the TICT state with twisted geometry, while the B band was derived from the localized excited (LE) state or the ICT state with planar geometry.[31,32] The solvent-dependent transition dipole moment (μ) values further support the polarity-regulated charge separation, leading to a more pronounced CT/TICT character (Fig. 3b–d and Table S4). The Lippert–Mataga analysis was further performed separately using the LE/ICT and TICT emission bands. The dipole-moment change ($\Delta\mu$) between S_0 and S_1 derived from the A band is significantly larger than that obtained from the B band, indicating that the TICT state possesses a more pronounced charge-separate character (Fig. 3b–d). Subsequently, the fluorescence intensity ratio (I_A/I_B) for the A and B bands was calculated based on the fluorescence profile in acetonitrile, showing an increasing trend from **QL-CHO** to **N-COOMe** (Fig. 3e). Specifically, the ratio increased from 0.11 for **Pyr-CHO** to 7.69 for **N-COOMe**, suggesting that the fluorescence in **N-COOMe** is more prominently attributed to the TICT state. Moreover, it was found that **N-COOMe** had a significantly stronger dependence of fluorescence on viscosity compared to other **SBLs**, which is consistent with its more prominent TICT character (Fig. S21–S23). Based on these findings, it can be concluded that the trend in the generation of the TICT state of **SBLs** is largely in agreement with that observed in the phosphorescence lifetimes and quantum yield of **SBL@PVAs** (Fig. 3e). The control compounds, **O-CO** and **S-CO**, containing methoxy or methylthio units instead of the dialkylamino group, displayed no effective OURTP in the PVA matrix. This indicates that the dialkylamino group, a typical TICT-capable moiety, is essential for enabling the OURTP behavior (Fig. S24 and Table S5). Thus, the attenuation in both the steric hindrance of the EDGs and the electron-withdrawing strength of the EWGs from **QL-CHO** to **N-COOMe** is expected to have facilitated the rotation of the dialkylamino group. This, in turn, influences the TICT state and thereby optimizes the OURTP properties.

To further explore the mechanisms underlying the positive correlation between the TICT formation capacity and OURTP enhancement in **SBL@PVAs**, density functional theory (DFT) and time-dependent DFT (TD-DFT) calculations were performed on these **SBLs** at the PBE0/Def2-TZVP level (Table S6). First, the potential energy of the lowest singlet excited state (S_1)

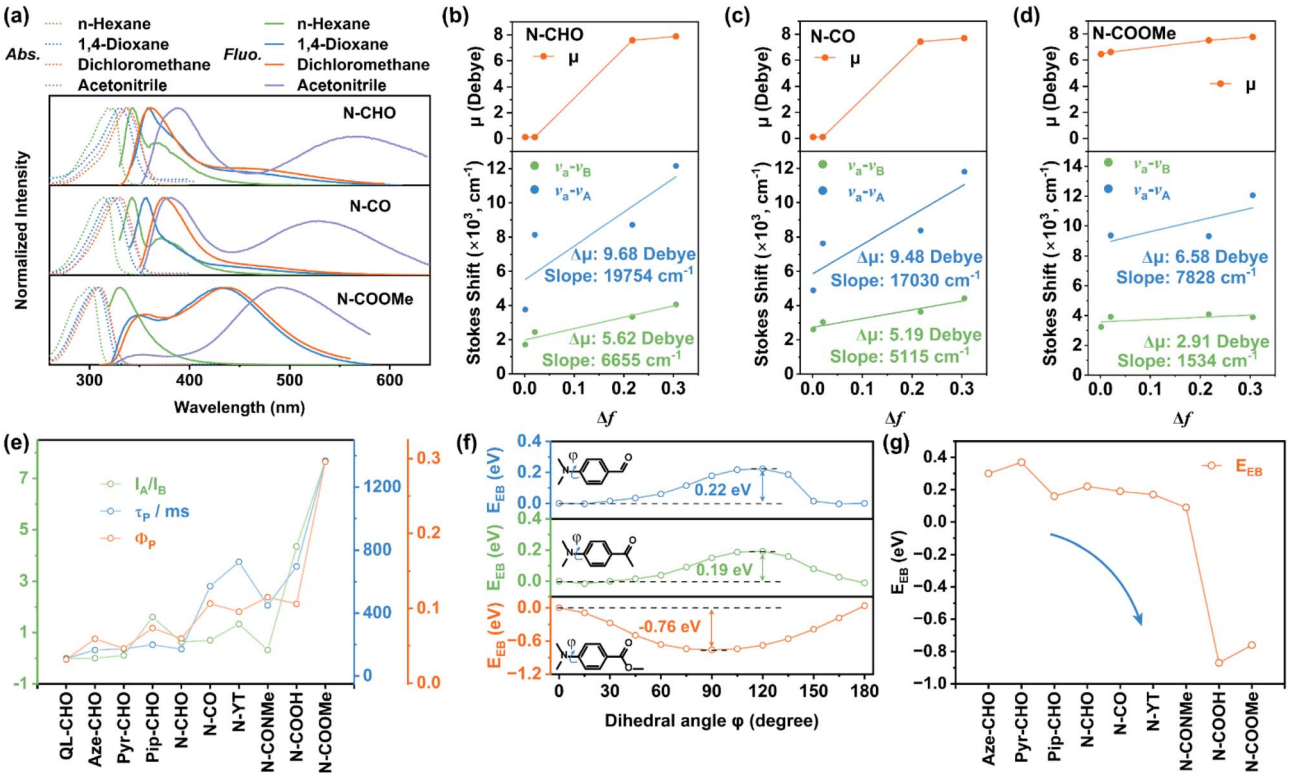

Fig. 3 (a) The absorption and fluorescence spectra of **N-CHO**, **N-CO**, and **N-COOMe** in different solvents, $C = 5 \times 10^{-5}$ mol L^{-1}. The S_0 to S_1 transition electric dipole moment (μ, top) and the relationships between the Stokes shift and Δf (bottom) for (b) **N-CHO**, (c) **N-CO**, and (d) **N-COOMe**. ν_a, ν_A, and ν_B: the wavenumber of the absorption maximum, A-band emission maximum, and B-band emission maximum, respectively. (e) The trends in the ratio of fluorescence intensity (I_A/I_B), phosphorescence lifetime, and phosphorescence quantum yield for the **SBLs**. (f) The E_{EB} of the optimized S_1 for **N-CHO** (top), **N-CO** (middle), and **N-COOMe** (bottom) with different φ values between the benzene ring and the EDGs. (g) The trends of E_{EB} of the optimized S_1 for the **SBLs**.

and ground state (S_0) was calculated as a function of the dihedral angle (φ) between the benzene ring and the EDGs (Tables S7 and S8). It was found that the S_1 potential energy decreased for **N-COOMe** and **N-COOH** with the increase of φ from 0° to 90°, whereas it increased for the other **SBLs** from 0° to 120°. In contrast, the S_0 potential energy exhibited an increasing trend for all **SBLs**. On this basis, the energy barriers (E_{EB}) associated with rotations of the EDGs were further evaluated. A lower E_{EB} suggests a greater propensity for TICT state formation.[33,34] It was found that the E_{EB} values in S_1 are lower than those in S_0, suggesting that twisted geometry is more readily accessible in S_1 for **SBLs** (Fig. 3f, S25 and S26). As shown in Fig. 3g, the E_{EB} of S_1 displays a clear downward trend from **Aze-CHO** to **N-COOMe**. The negative E_{EB} values observed for **N-COOMe** and **N-COOH** suggest that they were more prone to adopt twisted geometries characteristic of the TICT state in S_1, compared to others **SBLs**. This finding was consistent with the trend in solvent effects and further supports the correlation between the TICT formation capacity and the OURTP enhancement in **SBL@PVAs**. The electron paramagnetic resonance (EPR) measurements show a clear free-radical signal for **N-COOH@PVA**, while no obvious radical signal was observed for **N-COOMe@PVA** under UV irradiation (Fig. S27). Therefore, although **N-COOH** showed a smaller E_{EB}, it exhibited a shorter phosphorescence lifetime and lower quantum yield than **N-COOMe** in the PVA matrix (Table 1), presumably due to energy transfer from the triplet excited state to free radicals generated by **N-COOH@PVA** under UV irradiation.[35–37]

N-CHO, **N-CO**, and **N-COOMe** were selected as representative examples to further analyze their electronic configurations and excited-state characteristics in both planar and twisted geometries. Prior to the excited-state analysis, the electron-withdrawing ability of these acceptor groups was quantitatively evaluated using Hammett σ^- constants (Table S9).[38,39] The corresponding Hammett σ^- constants decrease from 1.126 to 0.874 and 0.636, confirming weakened acceptor strength from CHO to COMe and COOMe. Consistent with the Hammett σ^- constants, the decreased S_0 dipole moments and elevated LUMO energies further corroborate weakened donor–acceptor polarization and reduced electron-accepting ability. According to the El-Sayed rule, ISC processes, $^1(n, \pi^*)$ to $^3(\pi, \pi^*)$ or $^1(\pi, \pi^*)$ to $^3(n, \pi^*)$ transitions, are allowed for the generation of triplet excited states. Therefore, based on the hole–electron analysis and the proportion of n orbitals (α), it can be speculated that in the planar geometry, the $S_1 \rightarrow T_n$ ($n = 1$–4) transitions are allowed for **N-CHO** and **N-CO** due to the presence of hybrid (n, π^*) and (π, π^*) configurations in S_1 and triplet excited states (Fig. 4a, b, S28–S30, Tables S10–S13 and S15).[40,41] However, the transition is inefficient for **N-COOMe**

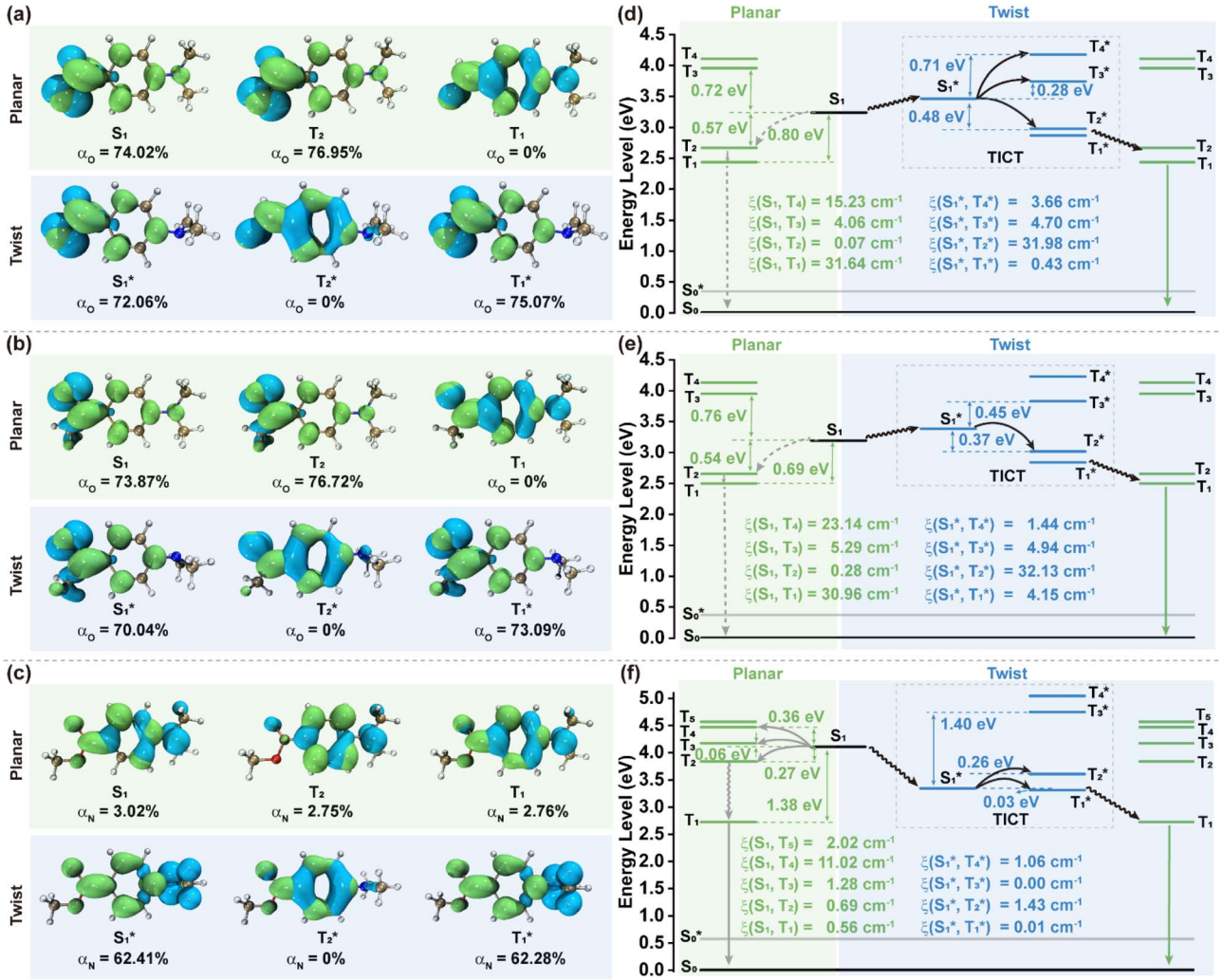

Fig. 4 The hole–electron analysis of (a) **N-CHO**, (b) **N-CO**, and (c) **N-COOMe** for their S_1, T_1, and T_2 excited states in planar geometries, as well as the S_1^*, T_1^*, and T_2^* excited states in twisted geometries, with the corresponding proportions of *n* orbitals (α). Calculated energy levels and spin–orbit coupling matrix elements (ξ) for (d) **N-CHO**, (e) **N-CO**, and (f) **N-COOMe**.

owing to their nearly pure (π, π^*) configurations in the S_1 and T_n (n = 1–4) states (Fig. 4c, S28, S31, Tables S12 and S17). By comparison, in twisted geometries ($\varphi = 120°$ for **N-CHO** and **N-CO**; $\varphi = 90°$ for **N-COOMe**), these analyses suggest that the transitions from S_1^* to T_n^* (n = 1–4) are allowed for all three **SBLs** (Fig. 4a–c, S28–31, Tables S10–S12, S14, S16 and S18). Since the ISC efficiency is governed by both the S_1–T_n energy gap and the SOC matrix element (ξ), energetically accessible triplet excited states with ΔE_{ST} values below or close to 0.37 eV were further examined, together with their corresponding ξ values. Higher-lying triplet states with larger ΔE_{ST} values may still contribute to the ISC to some extent, but their role is expected to be relatively minor. On this basis, compared with the planar geometry, the twisted geometry shows more efficient ISC and the subsequent triplet excited state population, which can be attributed to the reduced ΔE_{ST} and enhanced ξ (Fig. 4d–f). Although planar **N-COOMe** exhibits relatively small ΔE_{ST} values and appreciable ξ values for some channels, the similar (π, π^*) character of its S_1 and low-lying T_n states makes ISC less favorable according to the El-Sayed rule. In contrast, twisting provides more favorable orbital mixing together with reduced energy gaps and enhanced SOC, thereby facilitating ISC. These results underscore the critical role of the TICT character in governing the OURTP performance.

By exploiting the spectral overlap between the phosphorescence of **N-COOMe@PVA** and the absorption of the commercial fluorescent dye rhodamine B (**RhB**, Fig. S32a), we successfully engineered multicolor afterglow systems through triplet–singlet Förster resonance energy transfer (TS-FRET). By tuning the **N-COOMe/RhB** ratio in PVA films from 100 : 1 to 100 : 20, a clear afterglow shift from blue to orange was achieved (Fig. 5a, b and S32b). This shift was accompanied by a significant reduction in phosphorescence lifetime at 450 nm (from 1321 ms to 437 ms) and the emergence of millisecond-scale delayed fluorescence at 580 nm (Fig. 5c and d), providing unambiguous evidence of efficient TS-FRET and dynamic afterglow color tunability. Additionally, owing to the good processibility of PVA films, origami cranes were folded from **N-CO@PVA**, **N-COOMe@PVA**, and **N-COOMe/RhB@PVA**. Upon UV cessation, these origami

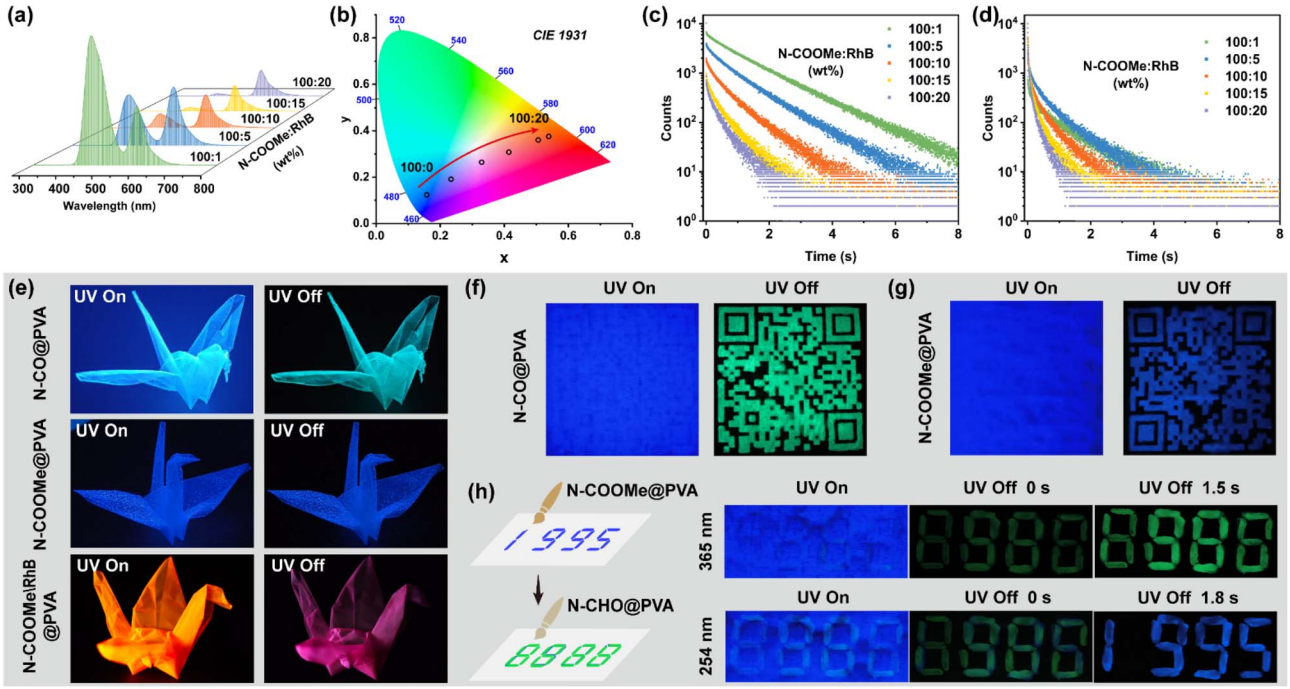

Fig. 5 (a) The delayed emission spectra (delay time = 5 ms), (b) CIE diagram of the delayed emission spectra, (c) the phosphorescence decay curves monitored at 450 nm, and (d) the delayed fluorescence decay curves monitored at 580 nm of the hybrid films at varying donor-to-acceptor ratios. (e) Photographs of the origami cranes folded using **N-CO@PVA** (λ_{ex} = 365 nm), **N-COOMe@PVA** (λ_{ex} = 254 nm), and **N-COOMe/RhB@PVA** (λ_{ex} = 254 nm) under UV irradiation and after turning off the UV light. Photographs of the QR code printed on paper using (f) **N-CO@PVA** (λ_{ex} = 365 nm) and (g) **N-COOMe@PVA** (λ_{ex} = 254 nm). (h) Photographs of multi-level encrypted information using **N-CHO@PVA** and **N-COOMe@PVA**.

structures exhibited bright cyan, blue, and purplish red afterglow emissions, highlighting their promising potential for use in flexible optoelectronic devices (Fig. 5e).

We further investigated the potential applications of the doped PVA films in information encryption. **N-CO@PVA** and **N-COOMe@PVA** aqueous solutions were then employed as anti-counterfeiting inks. A quick response (QR) code printed *via* screen printing using these inks was nearly invisible under UV light due to paper fluorescence but exhibited a clear green or blue afterglow upon UV removal, enabling successful smartphone scanning (Fig. 5f and g). In a time-dependent encryption demonstration, the number "2025" written with **N-CO@PVA** was overlaid with "8888" using **N-CHO@PVA**. Under 365 nm UV irradiation, the image transitioned from "8888" to "2025" over time due to their distinct phosphorescence lifetimes (Fig. S33). Similarly, when "1995" written with **N-COOMe@PVA** was covered by "8888" in **N-CHO@PVA**, and only "8888" was observed under 365 nm light, owing to weak phosphorescence emission from **N-COOMe@PVA** at this wavelength; however, under 254 nm UV light, the afterglow gradually shifted from green ("8888") to blue ("1995"), demonstrating enhanced security through wavelength-dependent dynamic encryption (Fig. 5h).

Conclusions

In summary, we demonstrate that precise control of TICT formation in **SBLs** enables significant OURTP enhancement within PVA matrices. Through strategic attenuation of steric hindrance in EDGs and electron-withdrawing potency in EWGs, we achieve a 12-fold phosphorescence lifetime extension (τ = 1368 ms) and 9-fold quantum yield (Φ_p = 29.6%) enhancement compared to systems with suppressed TICT state formation. Experimental results and theoretical calculations confirm that these improvements stem from TICT-mediated ΔE_{ST} reduction and SOC coefficient amplification. The PVA matrix further stabilizes triplet excitons through a rigid hydrogen-bonding network that blocks nonradiative decay. The outstanding OURTP performance and excellent processability make these **SBL@PVAs** promising candidates in afterglow displays and information encryption. Our "minimum effort, maximum effect" approach illustrates that sophisticated photophysical control can be achieved through minimalist structural changes, marking a departure from conventional complex multicomponent systems.

Author contributions

Wu-Jie Guo: conceptualization, investigation, methodology, data curation, formal analysis, validation, visualization, writing – original draft, writing – review and editing; Shirong Yan: investigation, validation, visualization, writing – original draft, formal analysis; Shihao Xu: investigation, validation; Tongfei Qi: investigation, validation; Hui-Qing Peng: funding acquisition, project administration, writing – review and editing, supervision, resources, conceptualization.

Conflicts of interest

There are no conflicts to declare.

Data availability

CCDC 2519407, 2518935 and 2519406 (**N-CHO**, **N-CO** and **N-COOMe**) contain the supplementary crystallographic data for this paper.[42a–c]

The experimental data associated with this article have been provided in supplementary information (SI). Supplementary information: experimental details, synthetic procedures, characterization data, theoretical calculation details, and additional figures and tables. See DOI: https://doi.org/10.1039/d6sc02382g.

Acknowledgements

H.-Q. Peng thanks the National Natural Science Foundation of China (22571012 and 22105016) and the National Key R&D Program of China (2022YFA1505900). This work was supported by the Interdisciplinary Research Center of Beijing University of Chemical Technology (No. XK2025-05).

Notes and references

1 W. Zhao, Z. He and B. Z. Tang, *Nat. Rev. Mater.*, 2020, **5**, 869–885.
2 Z. An, C. Zheng, Y. Tao, R. Chen, H. Shi, T. Chen, Z. Wang, H. Li, R. Deng, X. Liu and W. Huang, *Nat. Mater.*, 2015, **14**, 685–690.
3 Kenry, C. Chen and B. Liu, *Nat. Commun.*, 2019, **10**, 2111.
4 X.-Q. Liu, K. Zhang, J.-F. Gao, Y.-Z. Chen, C.-H. Tung and L.-Z. Wu, *Angew. Chem., Int. Ed.*, 2020, **59**, 23456–23460.
5 A. Cheng, H. Su, X. Gu, W. Zhang, B. Zhang, M. Zhou, J. Jiang, X. Zhang and G. Zhang, *Angew. Chem., Int. Ed.*, 2023, **62**, e202312627.
6 J.-X. Wang, H. Zhang, L.-Y. Niu, X. Zhu, Y.-F. Kang, R. Boulatov and Q.-Z. Yang, *CCS Chem.*, 2020, **2**, 1391–1398.
7 D. Chen, X. Guo, X. Sun, X. Feng, K. Chen, J. Zhang, Z. Zhu, X. Zhang, X. Liu, M. Liu, L. Li and W. Xu, *Exploration*, 2024, **4**, 20230166.
8 Y. Wang, J. Yang, M. Fang, Y. Yu, B. Zou, L. Wang, Y. Tian, J. Cheng, B. Z. Tang and Z. Li, *Matter*, 2020, **3**, 449–463.
9 G. Baryshnikov, B. Minaev and H. Agren, *Chem. Rev.*, 2017, **117**, 6500–6537.
10 G. Farias, C. A. M. Salla, M. Aydemir, L. Sturm, P. Dechambenoit, F. Durola, B. de Souza, H. Bock, A. P. Monkman and I. H. Bechtold, *Chem. Sci.*, 2021, **12**, 15116–15127.
11 J. X. Wang, Y. G. Fang, C. X. Li, L. Y. Niu, W. H. Fang, G. Cui and Q. Z. Yang, *Angew. Chem., Int. Ed.*, 2020, **59**, 10032–10036.
12 F. L. Ma, B. Wu, S. W. Zhang, J. H. Jiang, J. H. Shi, Z. Y. Ding, Y. Zhang, H. Z. Tan, P. Alam, J. W. Y. Lam, Y. Xiong, Z. Li, B. Z. Tang and Z. Zhao, *J. Am. Chem. Soc.*, 2025, **147**, 10803–10814.
13 W.-J. Guo, S. R. Yan, L. Chen, L. Qiao, S. H. Xu, T. F. Qi, B. Liu and H.-Q. Peng, *Adv. Funct. Mater.*, 2024, **34**, 2406888.
14 J.-L. Yu, Z. Chen, Y.-Q. Zhu, Y.-L. Jin, X. Wang, M.-X. Wu, X.-H. Wang and Y.-W. Yang, *Aggregate*, 2024, **5**, e562.
15 J. Zhao, L. Xu, Y. Meng, B. Xu and H. Cong, *Aggregate*, 2026, **7**, e70341.
16 D. Cui, L. Zhang, J. Zhang, W. Li, J. Chen, Z. Guo, C. Sun, Y. Wang, W. Wang, S. Li, W. Huang, C. Zheng and R. Chen, *Angew. Chem., Int. Ed.*, 2024, **63**, e202411588.
17 T. Wang, Z. Hu, X. Nie, L. Huang, M. Hui, X. Sun and G. Zhang, *Nat. Commun.*, 2021, **12**, 1364.
18 X.-F. Wang, H. Xiao, P.-Z. Chen, Q.-Z. Yang, B. Chen, C.-H. Tung, Y.-Z. Chen and L.-Z. Wu, *J. Am. Chem. Soc.*, 2019, **141**, 5045–5050.
19 G. M. Wang, X. F. Chen, Y. Zeng, X. Li, X. P. Wang and K. K. Zhang, *J. Am. Chem. Soc.*, 2024, **146**, 24871–24883.
20 H. Zeng, H. Li, P. Zhen, J. Zhou, B. Xu, G. Shi, Y. Zhang, Z. Chi and C. Liu, *Chem. Sci.*, 2025, **16**, 9169–9177.
21 C. Wang, W. Chi, Q. Qiao, D. Tan, Z. Xu and X. Liu, *Chem. Soc. Rev.*, 2021, **50**, 12656–12678.
22 J. T. Buck, A. M. Boudreau, A. DeCarmine, R. W. Wilson, J. Hampsey and T. Mani, *Chem*, 2019, **5**, 138–155.
23 M. Lv, Y. Yu, M. E. Sandoval-Salinas, J. Xu, Z. Lei, D. Casanova, Y. Yang and J. Chen, *Angew. Chem., Int. Ed.*, 2020, **59**, 22179–22184.
24 C. Chen, R. Huang, A. S. Batsanov, P. Pander, Y. T. Hsu, Z. Chi, F. B. Dias and M. R. Bryce, *Angew. Chem., Int. Ed.*, 2018, **57**, 16407–16411.
25 Z. R. Grabowski, K. Rotkiewicz and W. Rettig, *Chem. Rev.*, 2003, **103**, 3899–4032.
26 Z. Ye, W. Yang, C. Wang, Y. Zheng, W. Chi, X. Liu, Z. Huang, X. Li and Y. Xiao, *J. Am. Chem. Soc.*, 2019, **141**, 14491–14495.
27 K. Zhang, L.-Y. Peng, X.-X. Liu, X. Xu, W.-H. Fang, G. Cui, Y.-Z. Chen, C.-H. Tung and L.-Z. Wu, *Angew. Chem., Int. Ed.*, 2023, **62**, e202300927.
28 D. Li, Y. Yang, J. Yang, M. Fang, B. Z. Tang and Z. Li, *Nat. Commun.*, 2022, **13**, 347.
29 Z. Zhou, H. Wang, J. Yao, T. Wang, J. Liu, X. Cao, Q. Feng, B. Yue, D. Wang, J. Wang and H. Huang, *Aggregate*, 2026, **7**, e70296.
30 Y. Lang, J. Sun, M. Jiang, Q. Jiang, Y. Du, F. Wang, J. Zhou, G. Shi, B. Xu and C. Liu, *Chem. Sci.*, 2026, **17**, 9098–9107.
31 R. K. Guo, N. Kitamura and S. Tazuke, *J. Phys. Chem.*, 1990, **94**, 1404–1408.
32 C. Wang, W. Jiang, D. Tan, L. Huang, J. Li, Q. Qiao, P. Yadav, X. Liu and Z. Xu, *Chem. Sci.*, 2023, **14**, 4786–4795.
33 C. Wang, Q. Qiao, W. Chi, J. Chen, W. Liu, D. Tan, S. McKechnie, D. Lyu, X.-F. Jiang, W. Zhou, N. Xu, Q. Zhang, Z. Xu and X. Liu, *Angew. Chem., Int. Ed.*, 2020, **59**, 10160–10172.
34 X. Fang, Q. Qiao, Z. Li, H.-K. Li, Y. Huang, D. Hou, J. Chen, N. Xu, K. An, W. Jiang, Y. Tao, P. Bao, Y. Zhang, Z. Wu, X. Liu and Z. Xu, *J. Am. Chem. Soc.*, 2025, **147**, 22253–22267.
35 Y. Yang, J. Wang, J. Yang, L. Tong, D. Li, Y. Yang, M. Fang and Z. Li, *Angew. Chem., Int. Ed.*, 2023, **62**, e202218994.

36 Y. R. Li, G. Baryshnikov, C. G. Xu, H. Agren, L. L. Zhu, T. Yi, Y. L. Zhao and H. W. Wu, *Angew. Chem., Int. Ed.*, 2021, **60**, 23842–23848.
37 S. Chen, M. Shan, Z. Chen, Y. Meng, X. Wang, J. Yang, M. Fang and Z. Li, *Angew. Chem., Int. Ed.*, 2026, **65**, e9313527.
38 C. Hansch, A. Leo and R. W. Taft, *Chem. Rev.*, 1991, **91**, 165–195.
39 J. E. Leffler and E. Grunwald, *Rates and Equilibria of Organic Reactions*, Wiley, New York, 1963.
40 W. J. Zhao, Z. K. He, J. W. Y. Lam, Q. Peng, H. L. Ma, Z. G. Shuai, G. X. Bai, J. H. Hao and B. Z. Tang, *Chem*, 2016, **1**, 592–602.
41 H. Ma, Q. Peng, Z. An, W. Huang and Z. Shuai, *J. Am. Chem. Soc.*, 2018, **141**, 1010–1015.
42 (*a*) CCDC 2519407: Experimental Crystal Structure Determination, 2026, DOI: 10.5517/ccdc.csd.cc2qkn65; (*b*) CCDC 2518935: Experimental Crystal Structure Determination, 2026, DOI: 10.5517/ccdc.csd.cc2qk4zf; (*c*) CCDC 2519406: Experimental Crystal Structure Determination, 2026, DOI: 10.5517/ccdc.csd.cc2qkn54.